nature communications

Article

https://doi.org/10.1038/s41467-024-52526-9

Latent porosity of planar tris(phenylisoxazolyl)benzene

Received: 21 September 2023

Accepted: 11 September 2024

Published online: 27 September 2024

Check for updates

Yudai Ono[1,2], Takehiro Hirao[1], Naomi Kawata[3] & Takeharu Haino[1,2]

Interest in developing separation systems for chemical entities based on crystalline molecules has provided momentum for the fabrication of synthetic porous materials showing selectivity in molecular encapsulation, such as metal-organic frameworks, covalent organic frameworks, hydrogen-bonded organic frameworks, zeolites, and macrocyclic molecular crystals. Among these, macrocyclic molecular crystals have generated renewed interest for use in separation systems. Selective encapsulation relies on the sizes, shapes, and dimensions of the pores present in the macrocyclic cavities; thus, non-macrocyclic molecular crystals with high selectivity for molecular encapsulation via porosity-without-pore behaviors have not been studied. Here, we report that planar tris(phenylisoxazolyl)benzene forms porous molecular crystals possessing latent pores exhibiting porosity-without-pore behavior. After exposing the crystals to complementary guest molecules, the latent pores encapsulate *cis*- and *trans*-decalin while maintaining the structural rigidity responsible for the high selectivity. The encapsulation via porosity without pores is a kinetic process with remarkable selectivity for *cis*-decalin over *trans*-decalin with a *cis*-/*trans*-ratio of 96:4, which is confirmed by single-crystal X-ray diffraction and powder X-ray diffraction analyses. Hirshfeld surface analysis and fingerprint plots show that the latent intermolecular pores are rigidified by intermolecular dipole–dipole and π−π stacking interactions, which determines the remarkable selectivity of molecular recognition.

Porous materials comprise a diverse subset of molecular ensembles, such as metal-organic frameworks (MOFs)[1–4], covalent organic frameworks (COFs)[5–7], hydrogen-bonded organic frameworks (HOFs)[8–10], and zeolites[11–13]. The selectivities of MOFs, COFs, HOFs, and zeolites in molecular adsorption are determined by the sizes, shapes, and dimensions of the pores that are tightly retained in the crystalline structures. Therefore, porous materials have often been used for nonheat-driven separations in industry[14].

Macrocyclic molecules often form porous crystals in which various guest molecules are adsorbed within molecular cavities[15–21]. In macrocyclic molecular crystals, porosity-without-pores[22] behavior has often been reported. The macrocyclic molecular cavities in the solvent-free crystalline state are occupied by interpenetrating structures or collapse to reduce the surface area; therefore, the internally quenched cavities result in latent pores with the loss of porosity. The latent pores remain dormant and are restored by encapsulating complementary guest molecules. Thus, guest encapsulation is primarily restricted by the sizes, shapes, and dimensions of the latent pores. For example, calix[n]arene crystals prepared under vacuum at high temperature contain no mappable pores; however, when they are exposed to liquids and/or vapors, a single-crystal to single-crystal (SCSC) transition[23,24] is observed to form crystals containing guest molecules

[1]Department of Chemistry, Graduate School of Advanced Science and Engineering, Hiroshima University, 1-3-1 Kagamiyama, Higashi-Hiroshima, Hiroshima 739-8526, Japan. [2]International Institute for Sustainability with Knotted Chiral Meta Matter (WPI-SKCM²), Hiroshima University, 2-313 Kagamiyama, Higashi-Hiroshima, Hiroshima 739-0046, Japan. [3]Natural Science Center for Basic Research and Development (N-BARD), Hiroshima University, 1-3-1 Kagamiyama, Higashi-Hiroshima, Hiroshima 739-8526, Japan. e-mail: haino@hiroshima-u.ac.jp

within newly emerged pores, for which the sizes, shapes, and dimensions of the macrocyclic pores produce selective encapsulation[25–33].

In contrast, extrinsic intermolecular pores are frequently found in nonmacrocyclic molecular crystals. Close-packed molecular compartments preferentially reduce the surface area and maximize favorable intermolecular interactions in the crystalline state[34]; thus, sterically bulky three-dimensional structures, which encapsulate small guest molecules, are required to maintain residual voids as extrinsic intermolecular pores[35–38]. However, porosity-without-pore behavior with selective guest encapsulation is uncommon in nonmacrocyclic molecular crystals due to a lack of structurally determined latent pores. Thus, it remains challenging to establish porosity-without-pore behavior in selective guest encapsulation using nonmacrocyclic molecular crystals.

Tris(phenylisoxazolyl)benzene derivatives are planar molecules that form stacked supramolecular polymers through a combination of dipole–dipole interactions and π–π stacking interactions[39]. We envisioned that the two intermolecular interactions would determine the molecular arrangement of flat molecule **1** (Supplementary Figs. 1 and 2) in the crystalline state to generate well-defined latent pores (Fig. 1). Herein, we report stereoselections in the encapsulation of *cis*-decalin from a *cis*-/*trans*-decalin mixture based on planar tris(phenylisoxazole) benzene derivative **1** via porosity-without-pore behavior.

Results

Characterization of $CHCl_3$@1, 1α, 1β, and mixed-phase state

Tris(phenylisoxazolyl)benzene **1** showed good crystallinity with $CHCl_3$. X-ray diffraction-grade single crystals of $CHCl_3$@**1** with the *C*2/*c* space group were grown by slow evaporation of chloroform at room temperature (Fig. 2a and Supplementary Fig. 3). Two molecules of **1** formed a pair (colored in red in Fig. 2a), in which alternating deposition of the isoxazole rings caused the local dipole moments of isoxazoles to cancel each other out (Fig. 2b)[40]. The pairs were slip-stacked to form columnar assemblies with an interplanar distance of 3.4 Å (Fig. 2c)[41]. In the stacked structures, the remaining two isoxazole rings were slightly tilted to facilitate head-to-tail dipole–dipole interactions along the stacking direction. Figure 2a and d illustrate another pair, comprising two molecules of **1** colored in purple, which adopted a perpendicular arrangement with a center-to-center aromatic ring distance of 14.6 Å and an intermolecular dihedral angle of 78.6°; a pore enclosed a pair of chloroform molecules. The size, shape, and dimension of the pores were fitted to the exterior of the paired chloroform molecules (Fig. 2d). The close contacts between **1** and the chloroform molecules determined by Hirshfeld surface analysis and the fingerprint plots are summarized in Fig. 2e and Supplementary Figs. 4 and 5. One of the two chloroform molecules in the porous cavity exhibited intermolecular Cl/H (55%), Cl/Cl (23%), H/C (6%), Cl/O (4%), and H/N (4%) contacts (Fig. 2f and Supplementary Fig. 5). The close contacts H($CHCl_3$)–C(**1**) and Cl($CHCl_3$)–H(**1**) suggested the presence of intermolecular CH/π and CH/Cl interactions in the crystal. Accordingly, the two chloroform molecules formed a molecular exterior, complementary to the interiors of the porous cavities in the crystal, where CH/π and CH/Cl interactions participated in the stabilization of the crystal structure of $CHCl_3$@**1**.

Heating a single crystal of $CHCl_3$@**1** at 60 °C under vacuum for 3 h induced an SCSC transition, which resulted in solvent-free single crystals of **1**α and **1**β (Fig. 3a, b and Supplementary Figs. 6–8) (see the Methods section for the detection of the two phases). The space groups of the single crystals **1**α and **1**β were *Cc* and $Pca2_1$, respectively, and no apparent pores were found, which was confirmed by N_2 sorption experiments in the powder state (the estimated BET surface area was 2.52 $m^2\ g^{-1}$, Supplementary Fig. 9 and Supplementary Note 1). The

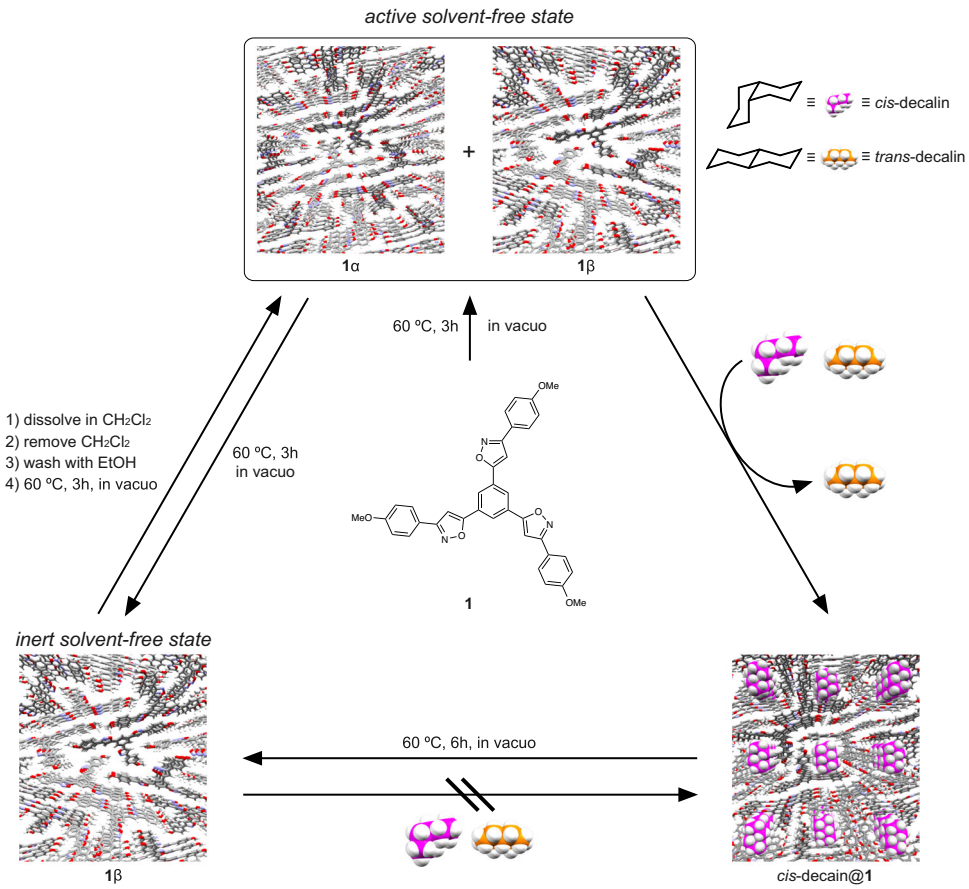

Fig. 1 | Graphical summary of the decalin encapsulation. Schematic representation of the sequential phase transitions of **1** in the solid state.

https://doi.org/10.1038/s41467-024-52526-9

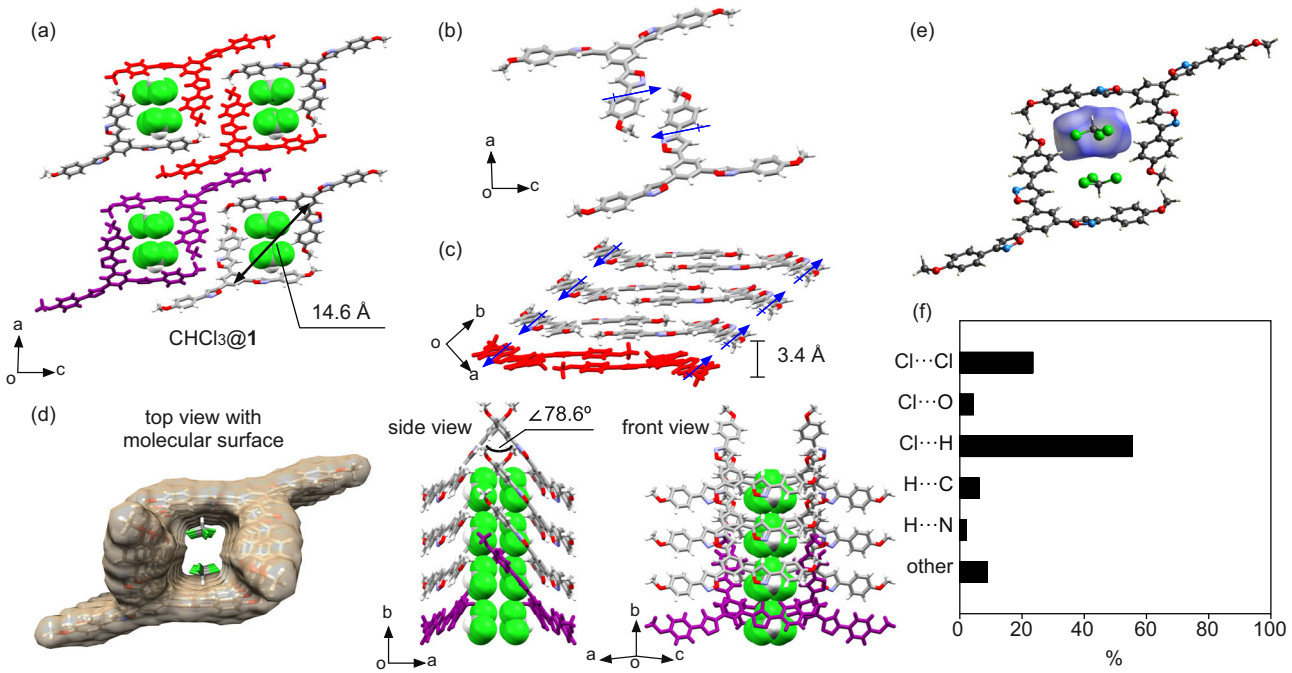

Fig. 2 | Studies of $CHCl_3$@1. a Single-crystal structure of $CHCl_3$@**1** along the crystallographic b-axis generated from a chloroform solution of **1**. **b** The structure of the dimeric pair of **1**, highlighted in red as depicted in **a**. The dipole moment induced by an isoxazole ring is shown as a blue arrow. **c** The single-crystal structure of $CHCl_3$@**1** along the crystallographic c-axis. The stacked structure comprises a pair of **1**, which is highlighted in red, as depicted in **a**. **d** Top, side, and front views of the single-crystal structure of $CHCl_3$@**1**. The two perpendicularly arranged molecules of **1**, highlighted in purple, are stacked in piles. The pair of chloroform molecules is encapsulated within the tubular pore. **e** Hirshfeld surface of $CHCl_3$@**1** mapped with d_{norm}. **f** Relative contributions to the Hirshfeld surface area for intermolecular contacts calculated from the structure are shown in **e**. The labels of the contact atoms denote Cl($CHCl_3$)–Cl($CHCl_3$), Cl($CHCl_3$)–O(**1**), Cl($CHCl_3$)–H(**1**), H($CHCl_3$)–C(**1**), and H($CHCl_3$)–N(**1**), from top to bottom. The labels indicate close contacts between other atoms; the details are shown in the Supplementary Information (Supplementary Fig. 5). Minimally disordered $CHCl_3$ molecules were omitted for clarity.

methoxyphenylisoxazole moiety in the single-crystal structure of **1**α was disordered and showed two orientations with occupancies of approximately 50%, and the center-to-center aromatic ring distance of the perpendicularly arranged pair of **1** was determined to be 10.0 Å with an intermolecular dihedral angle of 77.3° (Fig. 3a, c and Supplementary Figs. 8 and 10). Thus, pair **1** became closer and more squeezed to fill the residual pores. In addition, the rotational disorder of the isoxazole ring also reduced the size of the residual pores (Supplementary Fig. 8). In the single-crystal structure of **1**β, the paired molecules of **1** were arrayed along the crystallographic a-axis to form a densely packed structure without disorder (Fig. 3b, d, Supplementary Figs. 8 and 11). The center-to-center distance between the two nearest molecules of **1** was measured to be 12.7 Å. The two perpendicularly arranged molecules of **1** generated a dihedral angle of 76.2°. The pairs of **1** were squeezed and slightly rotated to quench the residual pore between the two molecules of **1** (Supplementary Fig. 8).

To study the phase behaviors in the powder state of **1**, an as-prepared **1** was heated at 60 °C under vacuum for 3 h. The resulting solvent-free powder was subjected to powder X-ray diffraction (PXRD) measurements, which illustrated a PXRD pattern that differed from that of the as-prepared powder **1**. The newly observed PXRD pattern was not consistent with the PXRD pattern for either the **1**α or **1**β phases simulated from their single-crystal structures (Supplementary Fig. 12). The PXRD pattern was reproduced with fair precision from a Rietveld refinement of the mixture of **1**α and **1**β based on the single-crystal structures of **1**α and **1**β and varying their ratio within the angular range of 2–50°. The Rietveld refinement allowed us to determine the unit cell parameters and *hkl* indices with a reasonable R_{wp} value of 7.27% (Fig. 3e, Supplementary Figs. 13). The unit cell parameters were consistent with those obtained from single crystals of **1**α and **1**β. The *hkl* indices were assigned to a mixture of space groups *Cc* and $Pca2_1$, which corresponded to those of the single crystals of **1**α and **1**β, respectively (Supplementary Tables 2, 3, and 7). Assuming that the solvent-free powder contained only the **1**α and **1**β phases, a 53:47 ratio between the **1**α and **1**β phases in the mixture was estimated with a two-phase model[42] involving a *Cc* phase and a $Pca2_1$ phase with Rigaku SmartLab Studio II software.

The thermodynamic stability of the solvent-free powder with the **1**α and **1**β phases was studied. When the as-prepared **1** was heated at 60 °C in vacuo for 6 h, the **1**α and **1**β phases were completely converted to the **1**β phase (Fig. 3e and Supplementary Fig. 14), suggesting that the **1**β phase is thermodynamically more stable than the **1**α phase, which is most likely a metastable phase.

Characterization of decalin@1

As-prepared **1** was dissolved in *cis*-decalin and in *trans*-decalin at 140 °C in glass vials. The resulting solutions were slowly cooled under ambient conditions, which generated X-ray diffraction-grade single crystals of *cis*-decalin@**1** and *trans*-decalin@**1**. The molecular arrangements of **1** within the crystal structures of both *cis*-decalin@**1** (Fig. 4a, c, Supplementary Figs. 15 and 17) and *trans*-decalin@**1** (Fig. 4b, d, Supplementary Figs. 16 and 17) were reasonably consistent with those in the single-crystal structures of $CHCl_3$@**1** (Fig. 2a). The two molecules of **1** adopted a perpendicular arrangement to form a pair, which was stacked in a columnar fashion. The *cis*- and *trans*-decalin molecules were located within pores formed by the columnar arrangement in the crystalline state.

Hirshfeld surface analysis and fingerprint plots of the single-crystal structures of *cis*-decalin@**1** revealed that approximately 80% of the hydrogen atoms in *cis*-decalin were located near the hydrogen atoms of surrounding molecule **1** and neighboring *cis*-decalin molecules, whereas 13%, 2%, and 5% of the hydrogen atoms in the *cis*-decalin molecule contacted the C, N, and O atoms of molecule **1**, respectively (Fig. 4e, f, Supplementary Figs. 18 and 19). The close contacts of H(*cis*-

https://doi.org/10.1038/s41467-024-52526-9

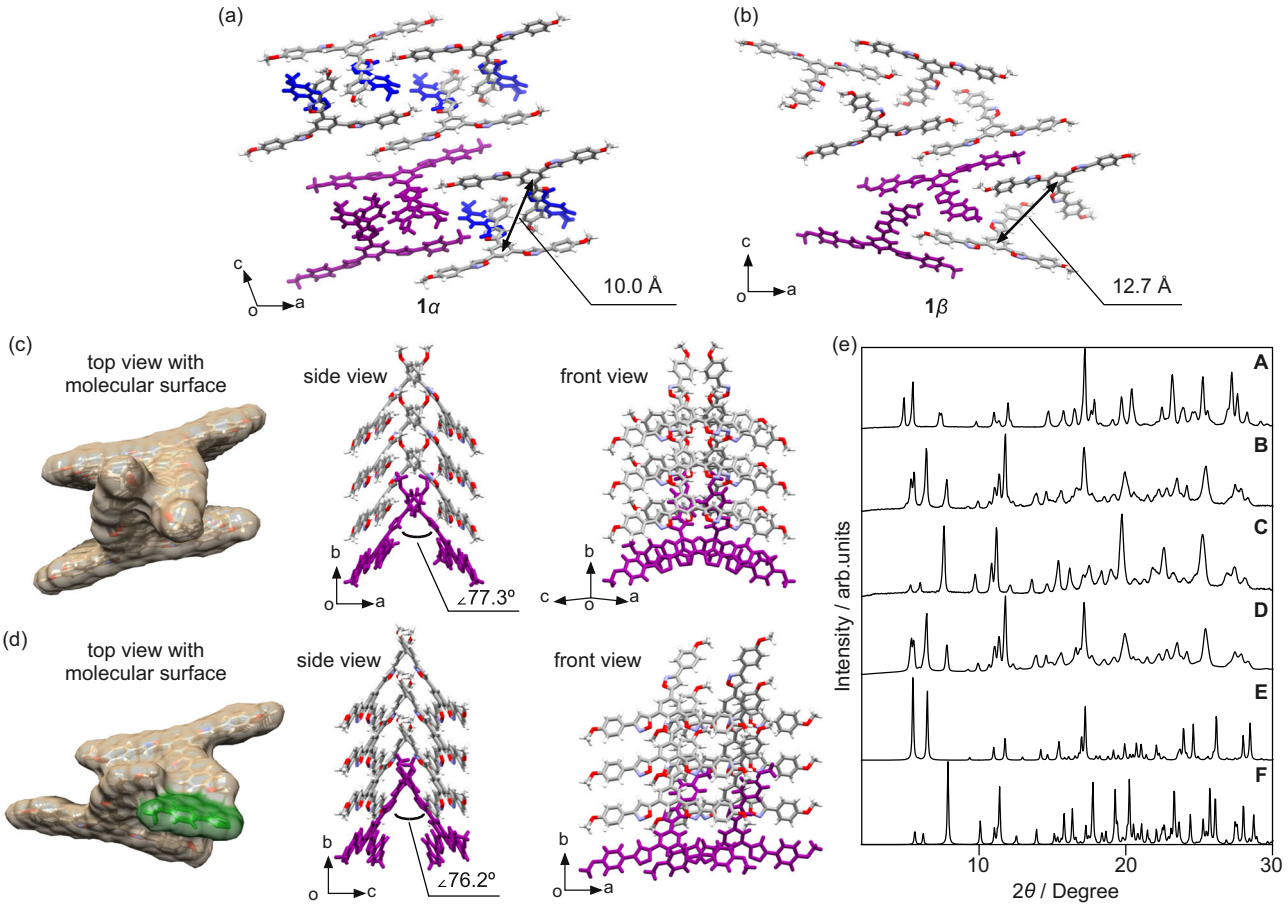

Fig. 3 | Studies of 1α and 1β. Single-crystal structures of (**a**) **1**α and (**b**) **1**β along the crystallographic b-axis. The disordered parts are highlighted in blue with an equal probability for the methoxyphenylisoxazole moiety. **c** Top, side, and front views of the single-crystal structure of **1**α. The two perpendicularly arranged molecules of **1**, highlighted in purple, are stacked in piles. No tubular pores were found. The disordered units were omitted for clarity. **d** Top, side, and front views of the single-crystal structure of **1**β. The two perpendicularly arranged molecules of **1**, highlighted in purple, are stacked in piles. No tubular pores were found. **e** PXRD patterns of powder **1** (A) as-prepared, (B) after heating at 60 °C for 3 h in vacuo, and (C) after heating at 60 °C for 6 h in vacuo. (D) PXRD pattern of a 53:47 mixture of the **1**α and **1**β phases estimated from Rietveld refinement. Simulated PXRD patterns shown in (E) and (F) were generated from the single crystals **1**α and **1**β, respectively.

decalin)–C(**1**), H(*cis*-decalin)–N(**1**), and H(*cis*-decalin)–O(**1**) atoms contributed to the formation of intermolecular CH/π or hydrogen bonds in the molecular structure. Concordant results were obtained with Hirshfeld surface analyses and fingerprint plots for the single-crystal structure of *trans*-decalin@**1**, as summarized in Fig. 4g, h and Supplementary Figs. 18 and 20. More than 80% of the hydrogen atoms in *trans*-decalin were in close contact with the hydrogen atoms of the surrounding **1** molecule and neighboring *trans*-decalin molecules, and the remaining 20% of the hydrogen atoms of the *trans*-decalin molecule were located near the C, N, and O atoms of molecule **1**. Accordingly, the formation of *cis*-decalin@**1** and *trans*-decalin@**1** was directed by the shape complementarity between the guests and the porous cavity formed in crystalline **1** during cocrystallization.

Common porous crystals often encapsulate and release their guests at the solid/liquid interface in thermodynamic equilibrium; thus, guest exchange is observed when porous crystals are exposed to guest molecules that are more complementary than those encapsulated in the pores[43,44]. To discuss the stabilities of the cocrystals, single crystals of *cis*-decalin@**1** and *trans*-decalin@**1** were soaked in *trans*-decalin and *cis*-decalin, respectively. Both specimens were left standing for two days under ambient conditions. No guest exchange was observed in the cocrystals (Supplementary Fig. 21), implying that large energy barriers prohibited in-and-out guest exchange at the solid/liquid interface. Accordingly, the guest encapsulation of **1** is most likely a kinetic process without any guest exchange[45].

Exposing a solvent-free powder with the **1**α and **1**β phases to *cis*- and *trans*-decalin vapors for 6 days in glass vessels resulted in new PXRD patterns (Fig. 4iA, B and Supplementary Fig. 22), consistent with those of *cis*-decalin@**1** and *trans*-decalin@**1** (Fig. 4iC, D, Supplementary Figs. 23 and 24), which were obtained by Rietveld refinements based on simulated PXRD patterns of single crystals of *cis*-decalin@**1** and *trans*-decalin@**1** (Fig. 4iE and F). Thus, the solvent-free powder with the **1**α and **1**β phases encapsulated decalin molecules to form crystals of *cis*-decalin@**1** and *trans*-decalin@**1** by opening the collapsed porous cavity between the two molecules of **1**. The *cis*-decalin@**1** and *trans*-decalin@**1** powders were exposed to *trans*- and *cis*-decalin vapors, respectively, for 6 days, but no discernible changes were observed in the PXRD patterns. The guest molecules in the *cis*-decalin@**1** and *trans*-decalin@**1** powders did not undergo exchange at the solid/vapor interface for at least 6 days, which was consistent with the results observed for the single crystals (Supplementary Fig. 25).

Selectivity in guest encapsulation

Cis- and *trans*-decalin molecules have the same elemental compositions; thus, stereoselective encapsulation of either *cis*- or *trans*-decalin requires shape complementarity between the guest molecules and the porous cavity. The stereoselective crystallization of **1** with the guest was studied. As-prepared **1** was dissolved in a 1:1 mixture of *cis*- and *trans*-decalin at 140 °C, which enabled cooling at room temperature under ambient conditions. X-ray diffraction-grade single crystals were

https://doi.org/10.1038/s41467-024-52526-9

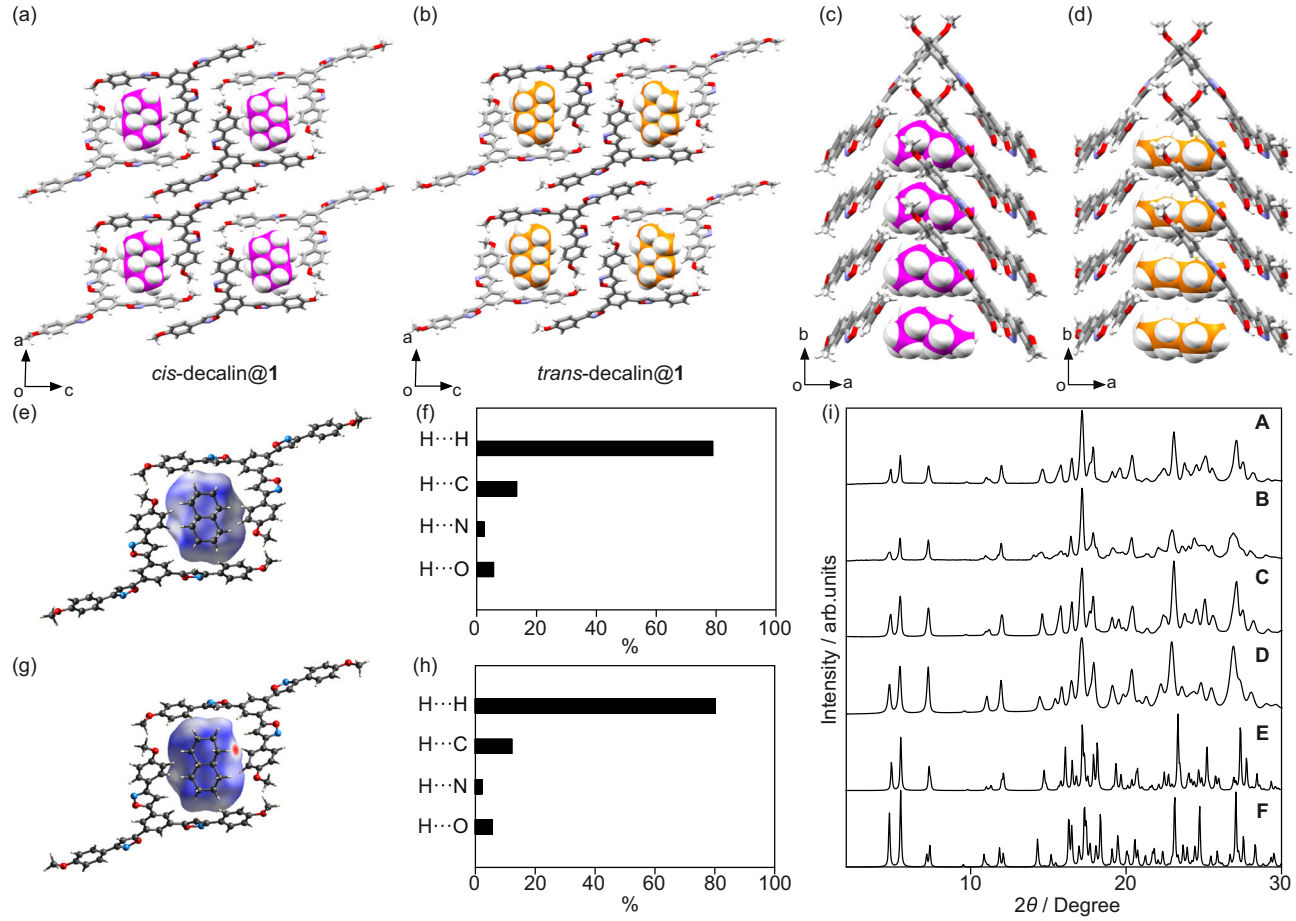

Fig. 4 | Studies of *cis*-decalin@1 and *trans*-decalin@1. Images of single-crystal structures of (**a**) *cis*-decalin@**1** and (**b**) *trans*-decalin@**1** along the crystallographic b-axis generated from the *cis*-decalin and *trans*-decalin solutions of **1**, respectively. **c** *Cis*-decalin and (**d**) *trans*-decalin encapsulation within the pores between two molecules of **1**. Hirshfeld surfaces of (**e**) *cis*-decalin@**1** and (**g**) *trans*-decalin@**1** mapped with d_{norm}. Relative contributions to the Hirshfeld surface area for intermolecular contacts calculated from the structures shown in (**f**) Panel *e* and (**h**) Panel *g*. The labels on the contact atoms denote H(decalin)−H(**1** or decalin), H(decalin)−C(**1**), H(decalin)−N(**1**), and H(decalin)−O(**1**), from top to bottom. (i) PXRD patterns for solvent-free powder with the **1**α and **1**β phases when exposed to (A) *cis*-decalin vapor and (B) *trans*-decalin vapor. PXRD patterns of (C) *cis*-decalin@**1** and (D) *trans*-decalin@**1** estimated with Rietveld refinement based on simulated PXRD patterns of (E) *cis*-decalin@**1** and (F) *trans*-decalin@**1** generated from their single-crystal structures.

obtained and subjected to single-crystal X-ray diffraction (SXRD) analysis. The crystal structure exhibited cocrystallization of **1** with *cis*-decalin (*cis*-decalin@**1**) (Supplementary Fig. 26), which indicated that the pores between two molecules of **1** were well defined and encapsulated by *cis*-decalin rather than *trans*-decalin. To determine the limit of selection (LOS), single crystals of **1** were grown from a 3:7 mixture, a 2:8 mixture, a 1:9 mixture, and a 0.1:9.9 mixture of *cis*- and *trans*-decalin. X-ray diffraction analyses of the single crystals based on the What is this? program[46] revealed that *cis*-decalin@**1** was selectively formed from the 3:7 mixture and the 2:8 mixture of *cis*- and *trans*-decalin (Supplementary Fig. 27). In contrast, *trans*-decalin@**1** formed single crystals when grown in a 1:9 mixture of *cis*- and *trans*-decalin. Accordingly, the formation of single-crystal *cis*-decalin@**1** was preferred even in the presence of excess *trans*-decalin.

The vapor adsorbed by **1** resulted in stereoselective encapsulation. The solvent-free powder with the **1**α and **1**β phases was prepared by heating the as-prepared **1**, which was exposed to a vaporous *cis*-/*trans*-decalin mixture (1:1, w/w). A change in the PXRD pattern for solvent-free powder with the **1**α and **1**β phases was clearly observed when exposed to the vaporous *cis*-/*trans*-decalin mixture for 6 days. The PXRD pattern obtained from the *cis*-/*trans*-decalin mixture was fully consistent with that of **1** exposed to *cis*-decalin vapor (Fig. 5 and Supplementary Fig. 28). Although the vapor pressure of *trans*-decalin was reported to be slightly greater than that of *cis*-decalin[47], **1** selectively encapsulated *cis*-decalin from a vaporous *cis*-/*trans*-decalin mixture. To determine the LOS, a solvent-free powder with the **1**α and **1**β phases was exposed to vaporous (3:7, 1:9, 0.5:9.5, 0.4:9.6, 0.3:9.7, 0.2:9.8, and 0.1:9.9) *cis*-/*trans*-decalin mixtures (w/w) for 6 days (Supplementary Fig. 29). The formation of *cis*-decalin@**1** was indicated by the PXRD pattern after exposure to the vaporous 3:7, 1:9, and 0.5:9.5 *cis*-/*trans*-decalin mixtures, whereas the PXRD pattern for **1** exposed to vaporous 0.1:9.9 *cis*-/*trans*-decalin mixtures was not consistent with that of *cis*-decalin@**1**. Judging from a plot of the residual sum of squares (RSS) between the PXRD patterns of the mixtures and *cis*-decalin against the proportion of *cis*-decalin in the *cis*-/*trans*-decalin mixture, the selective formation of *cis*-decalin@**1** required at least 4 w/w% *cis*-decalin in the *trans*-decalin solution (Supplementary Fig. 30 and Table 1). It is striking that the encapsulation of a *cis*-decalin molecule into **1** was kinetically more favorable than that of a *trans*-decalin molecule, with an activation energy difference of approximately 1.6 kcal mol^{-1}. Time-dependent PXRD monitoring further suggested the encapsulation mechanism of **1**. The solvent-free powder with the **1**α and **1**β phases was exposed to vaporous *cis*-decalin, resulting in changes in the PXRD patterns (Fig. 6a and Supplementary Fig. 31). As the diffraction peaks attributed to the **1**α and **1**β phases gradually decreased, those of *cis*-decalin@**1** increased. The changes in intensity of PXRD peaks were plotted against time, which showed that the intensity of PXRD peaks of **1**α and **1**β decreased at approximately the

same ratio, while the intensity of those of *cis*-decalin@**1** increased with time (Fig. 6b and Supplementary Fig. 31). The sum of the normalized intensity of **1**α, **1**β, and *cis*-decalin@**1** was observed to be more than 0.9 at each time point, ruling out the presence of an intermediate phase. Thus, the solvent-free powder with the **1**α and **1**β phases was instantaneously converted to *cis*-decalin@**1** by the direct crystal-to-crystal phase transition.

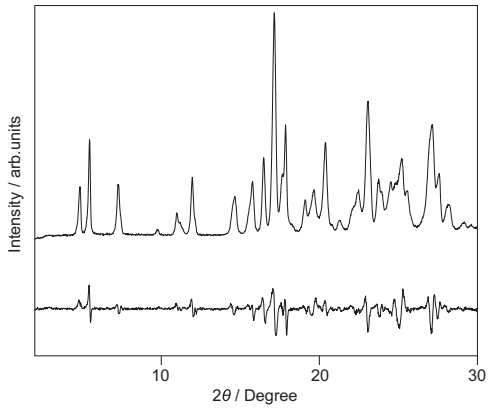

Fig. 5 | Selective *cis*-decalin encapsulation of 1. PXRD patterns for the solvent-free powder with the **1**α and **1**β phases after exposure to a vaporous 1:1 *cis*-/*trans*-decalin mixture. The bottom line represents the difference between the PXRD patterns for **1** after exposure to a vaporous 1:1 *cis*-/*trans*-decalin mixture and vaporous *cis*-decalin (Fig. 4iA).

Table 1 | Summary of the *cis*-/*trans*-selectivity of 1 for decalin encapsulation

	Mixing ratio (*cis*: *trans*)[a]					
	1:1	3:7	2:8	1:9	0.4:9.6	0.1:9.9
SXRD[b]	cis	cis	cis	trans	N/A	trans
PXRD[c]	cis	cis	N/A	cis	cis	trans-rich

[a]Adopted from the weight/weight ratio.
[b]Recrystallized from the cis-/trans-decalin mixture.
[c]Exposed to a vaporous cis-/trans-decalin mixture for 6 days.
The experimental data are shown in Supplementary Figs. 27 and 29.

To restore the guest-free powders for reuse, the powder *cis*-decalin@**1** was placed in a glass vial (capacity of 5 mL) and heated at 60 °C in vacuo. The complete removal of the *cis*-decalin molecule required heating for 6 h, resulting in a solvent-free powder with the **1**β phase (Fig. 7a and Supplementary Fig. 31). The removal of encapsulated solvent molecules was also observed in $CHCl_3$@**1** and *trans*-decalin@**1** by heating (Supplementary Fig. 32). When the solvent-free powder with the **1**β phase was exposed to a vaporous *cis*-/*trans*-decalin mixture (1:1, w/w) for 6 days, no discernible change in the PXRD pattern was observed, which suggested that powder **1**β did not encapsulate a decalin molecule (Fig. 7a and Supplementary Fig. 31). Thus, the solvent-free powder with the **1**β phase is in a solvent-free inert state (Fig. 1). Given that solvent-free powder with the **1**α and **1**β phases encapsulate decalin molecules, the presence of the **1**α phase most likely promotes the inert **1**β phase to facilitate the encapsulation of decalin molecules. The **1**β-rich solvent-free powder with a **1**α:**1**β ratio of 2:98 (estimated by Rietveld refinement with an R_{wp} value of 9.07%) was subjected to a guest encapsulation experiment by exposure to a vaporous *cis*-/*trans*-decalin mixture (1:1, w/w) for 6 days (Fig. 7b and Supplementary Fig. 33). The resulting powders contained *cis*-decalin@**1** and **1**β at a ratio of 29:71, respectively, as estimated by Rietveld refinement, with an R_{wp} value of 8.45% (Fig. 7b and Supplementary Fig. 34). The amount of *cis*-decalin@**1** formed is significantly greater than that of the **1**α phase. Thus, all of the **1**α phase was consumed in the encapsulation of *cis*-decalin, while the **1**α phase promoted a portion of the **1**β phase to encapsulate decalin molecules yielding *cis*-decalin@**1**. To detail the transition from the solvent-free powder with the **1**α and **1**β phases to *cis*-decalin@**1**, the solvent-free powder with the **1**α and **1**β phases (**1**α:**1**β = 53:47) was mixed with **1**β in a ratio of 8:2, which is herein defined as post-mixed powder whereas the solvent-free powder with **1**α and **1**β obtained by heating the as-prepared **1** is defined as the pre-mixed powder, in the following section, where above-mentioned all the solvent-free powder with the **1**α and **1**β phases denote pre-mixed powder. The resulting post-mixed powder (**1**α:**1**β = 42:58) was ground by a mortar and pestle. The post-mixed solvent-free powder with the **1**α and **1**β phases was exposed to a vaporous 1:1 *cis*-decalin mixture for 6 days, which resulted in the mixture of *cis*-decalin@**1** and **1**β left (Fig. 7c and Supplementary Fig. 31). This observation suggests that the pre-mixed state is crucial for the decalin encapsulation. It is most likely that the **1**α phase is in adequate interfacial contact with the **1**β phase in the pre-mixed powder, which promotes the **1**β phase to encapsulate decalin molecules. These results indicate that the pre-

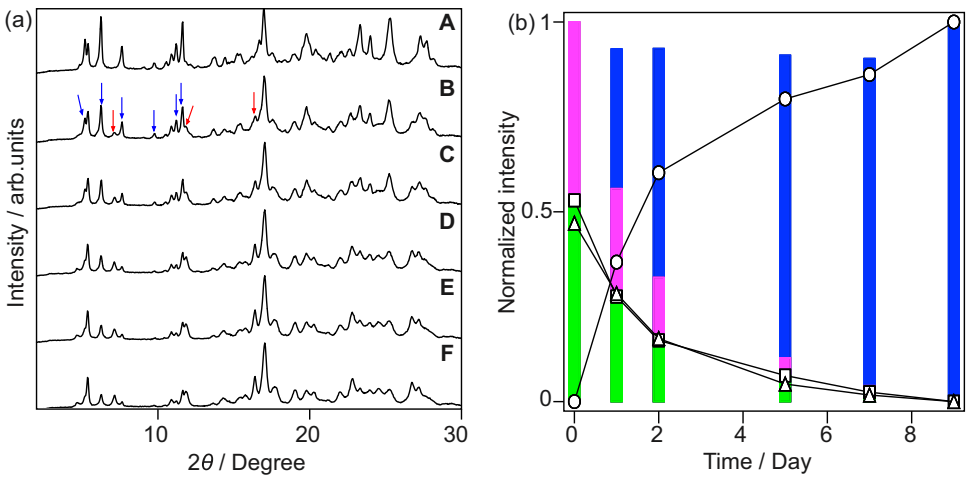

Fig. 6 | Time-dependent decalin encapsulation of 1. a Time-dependent changes in the PXRD pattern for the solvent-free powder with the **1**α and **1**β phases when exposed to a 1:1 mixture of vaporous *cis*- and *trans*-decalin for (A) 0 days, (B) 1 day, (C) 2 days, (D) 5 days, (E) 7 days, and (F) 9 days. The red and blue arrows in Panel **b** indicate increasing and decreasing trends, respectively. **b** Plot of normalized PXRD peak intensity of (square) **1**α (6.24°), (triangle) **1**β (7.62°), and (circle) *cis*-decalin@**1** (7.14°) against time. The bar graph indicates the sum of the normalized intensity, where green, magenta, and blue correspond to **1**α, **1**β, and *cis*-decalin@**1**, respectively.

https://doi.org/10.1038/s41467-024-52526-9

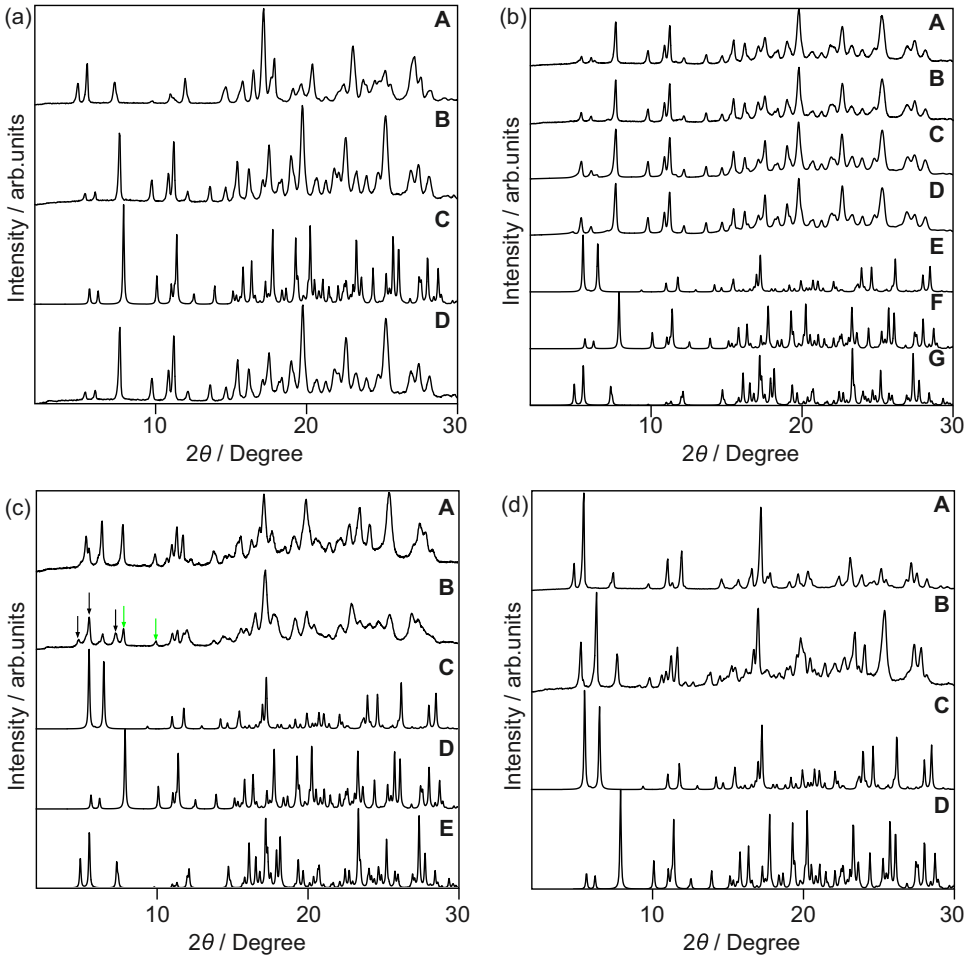

Fig. 7 | Decalin encapsulation behaviors of 1. a (A) PXRD pattern for *cis*-decalin@**1**. (B) PXRD pattern for *cis*-decalin@**1** shown in Panel **A** after heating at 60 °C for 6 h in vacuo. (C) Simulated PXRD pattern generated from single-crystal structure of **1**β. (D) PXRD pattern for the resulting powder shown in Panel **B** after exposure to a vaporous *cis*-/*trans*-decalin (1:1) mixture for 6 days. **b** (A) PXRD pattern for as-prepared **1** (80 mg) after heating at 60 °C for 3 h. (B) PXRD pattern for the resulting powder shown in Panel **A** after being exposed to a vaporous *cis*-/*trans*-decalin mixture (1:1, w/w) for 6 days (for detailed procedures, see the Methods section). (C) PXRD pattern of a mixture of **1**α and **1**β and (D) PXRD pattern of a mixture of *cis*-decalin@**1** and **1**β estimated by Rietveld refinement. Simulated PXRD patterns of (E) **1**α, (F) **1**β, and (G) *cis*-decalin@**1** generated from their single-crystal structures. **c** (A) PXRD pattern for the post-mixed powder with the **1**α and **1**β phases (**1**α:**1**β = 42:58). (B) PXRD pattern for the post-mixed powder shown in Panel **A** after exposure to vaporous *cis* -decalin for 6 days. The green and black arrows indicate peaks corresponding to **1**β and *cis* -decalin@**1**, respectively. Simulated PXRD patterns generated from single-crystal structure of (C) **1**α, (D) **1**β, (E) *cis* -decalin@**1**. **d** (A) PXRD pattern of the solvent-free powder with the **1**β phase after it was dissolved in CH_2Cl_2, concentrated in vacuo, washed with EtOH, and then dried in vacuo at room temperature. (B) PXRD pattern for the resulting powder shown in Panel **A** after heating at 60 °C for 3 h. Simulated PXRD patterns of (C) **1**α and (D) **1**β generated from their single-crystal structures.

mixed state with the **1**α and **1**β phases is crucial for the encapsulation of decalin molecules in the latent pore, where the **1**α phase most likely promotes a fair amount of the **1**β phase to encapsulate decalin molecules.

To reuse the inert powder with the **1**β phase, this powder was dissolved in CH_2Cl_2 with gentle heating in a water bath and then concentrated in vacuo. The resulting powder was washed with EtOH and then heated at 60 °C in vacuo for 3 h to yield the active solvent-free powder with the **1**α and **1**β phases, demonstrating the repeatability of the decalin encapsulation and release process (Fig. 7d and Supplementary Fig. 31).

Discussion

In summary, we report that planar tris(phenylisoxazolyl)benzene derivative **1** formed cocrystalline $CHCl_3$@**1**, which produced latent porous crystals of **1**α and **1**β. Although there were no viable pores in either the **1**α or **1**β phase, they favorably encapsulated *cis*-decalin over *trans*-decalin from a *cis*-/*trans*-mixture of decalin within the emerging pores, which was established through a combination of single-crystal X-ray diffraction and PXRD analyses. Hirshfeld surface analysis and fingerprint plots revealed that the selectivity of solvent encapsulation was driven by the sizes, shapes, and dimensions of the well-defined pores. The time-dependent PXRD monitoring of the solvent-free powder with the **1**α and **1**β phases upon exposure to vaporous *cis*-decalin revealed that the **1**α and **1**β phases were converted to *cis*-decalin@**1** by the direct crystal-to-crystal phase transition. Finally, the post-mix experiment revealed that the pre-mixed state of the **1**α and **1**β phases are crucial for the decalin encapsulation, leading to the conclusion that the **1**α phase is in adequate interfacial contact with the **1**β phase in the pre-mixed powder, which promotes the **1**β phase to encapsulate of the decalin molecules. Such a consideration of the guest encapsulation behavior should be useful to deepen the understanding of small molecules exhibiting the porosity-without-pore behavior.

In general, macrocyclic assemblies exhibit selectivity for guest binding within their cavities. The sizes, shapes, and dimensions of guest molecules must be complementary to the cavity interiors to achieve high selectivity in guest binding. On this basis, flat molecules

are hard to show selectivity in guest binding. Although flat molecule **1** resulted in solvent-filled pores, the perpendicular arrangement of two molecules of **1** rigidified the porous cavities via intermolecular interactions, which was confirmed by the fingerprint plot of $CHCl_3$@**1**, *cis*-decalin@**1**, and *trans*-decalin@**1** (Supplementary Figs. 5, 19, and 20). In fact, the size, shape, and dimension of the pores occupied by $CHCl_3$ in $CHCl_3$@**1** are consistent with those observed in *cis*-decalin@**1** and *trans*-decalin@**1**, which is characterized by the observation of the concordant void volumes within the unit cell of the pores of $CHCl_3$@**1**, *cis*-decalin@**1**, and *trans*-decalin@**1** (Supplementary Fig. 35), resulting in the excellent selectivity coming from the rigid feature of the porous cavity even though they are latent without guest molecules.

After heating of the crystals of **1**, the latent pores were retained and remained dormant. Upon exposing the crystals to complementary guest molecules, the latent pores encapsulated the guest molecules and maintain the structural rigidity responsible for the high selectivity. Accordingly, the active crystals of **1**α and **1**β possessed latent intermolecular pores, exhibiting porosity-without-pore behaviors. **1**α (Fig. 3a) ideally possesses porous cavity derived from the disordered moiety. However, N_2 adsorption experiments confirmed that solvent-free powder with the **1**α and **1**β phases is nonporous (Supplementary Fig. 9 and Supplementary Note 1). We thus conclude that porosity-without-pore is the most suitable description for the observed phenomenon. Although porosity-without-pore behaviors commonly require macrocyclic molecular structures with large molecular cavities, the simple, nonmacrocyclic, planar molecule **1** clearly exhibited porosity-without-pore behavior and remarkable stereoselectivity between *cis*-/*trans*-decalin. This work represents a potential advantage of using flat molecules as porous materials. The pores provided by the flat molecule do not collapse in response to environmental stimuli because intermolecular pores emerge only at the moment of guest molecule encapsulation. Thus, the present work is expected to set the stage for the creation of porous materials that show separation capability with improved environmental stress tolerance.

Methods

All reagents and solvents were commercial reagent grade and were used without further purification except where noted. Triethylamine (98.0%) and CH_2Cl_2 (98.0%) were purchased from Nacalai Tesque, Inc., JAPAN. Dry triethylamine and dry CH_2Cl_2 were obtained by distillation over KOH and CaH_2, respectively. 1,3,5-triethynylbenzene[48] and benzohydroximoyl chrolide[49] were synthesized according to reported procedures. ^{1}H and ^{13}C NMR spectra were recorded on a JEOL ECA-500 spectrometer. Chemical shifts were reported in the delta scale in ppm relative to residual chloroform (δ = 7.26 and 77.2 for ^{1}H and ^{13}C, respectively). High Resolution ESI mass spectrometry was performed using a Thermo Fisher Scientific LTQ Orbitrap XL hybrid FTMS. Melting points (M.p.) were measured with a Yanagimoto micro melting point apparatus. N_2 gas sorption experiment was performed on a BELSORP-maxII034VP-MZ (MicrotracBEL). X-ray crystallographic data were obtained with a Rigaku XtaLAB Synergy R, DW system, HyPix diffractometer. The crystals were kept at 100 K during data collection. Using Olex2[50], the structure was solved with the SHELXD[51] structure solution program using Dual Space or SHELXT[52] structure solution program using Intrinsic Phasing and refined with the SHELXL[53] refinement package using Least Squares minimization. The crystals were irradiated with Cu*K*α radiation (λ = 1.54184 Å).

Characterization

The synthesis and characterization of **1** are described in full detail in the Supplementary Information, which contains the ^{1}H NMR and ^{13}C NMR spectra of the compound.

Preparation of single crystals of $CHCl_3$@1

First, 1 mg of as-prepared **1** and 1 mL of commercial-grade $CHCl_3$ were mixed in a glass vial (capacity of 5 mL) at room temperature. The specimen was heated at 50 °C for 2 min by oil-bath heating without stirring under an open-air atmosphere. Then, the heater was turned off to reach room temperature. The diffraction grade of the single crystals increased as the temperature gradually decreased.

Preparation of single crystals of 1α and 1β

Approximately 50 single crystals of $CHCl_3$@**1** were randomly selected and placed on a glass plate by a metallic spatula. Then, the glass plate with the crystals was heated by a hot plate at 60 °C for 3 h in vacuo, resulting in diffraction-grade plates and block crystals corresponding to **1**α and **1**β, respectively. The crystals were separated by using a needle and subjected to SXRD analysis.

Preparation of single crystals of *cis*-decalin@1 and *trans*-decalin@1

As-prepared **1** (3 mg) and 2 mL of commercial grade *cis*- or *trans*-decalin were mixed in a glass vial (capacity of 5 mL) at room temperature. The specimens were heated at 140 °C for 5 min by heating in an oil bath with stirring under an open-air atmosphere. Then, the heater was turned off to reach room temperature. The diffraction grade of the single crystals increased as the temperature gradually decreased.

Hirshfeld surface analysis

Hirshfeld surface analysis was carried out using CrystalExplorer software (version 21.3)[54].

Rietveld refinement

Rietveld refinement was carried out using Rigaku SmartLab Studio II software (version 4.5.286.0). The initial crystallographic parameters were acquired from the single-crystal structures. The Rietveld refinement in this work was performed to assign *hkl* indices; thus, atomic coordinate refinements were excluded from the Rietveld refinement, resulting in relatively large *S* values that did not impact the authors' conclusions.

Preparation of solvent-free powders

First, 1.0 g of as-prepared **1** was placed in a glass vial (capacity of 50 mL), which was heated at 60 °C for 3 h in vacuo, resulting in a pre-mixed solvent-free powder with the **1**α and **1**β phases. The resulting mixture (80 mg) was placed in a glass vial (capacity of 5 mL), which was heated at 60 °C for 3 h in vacuo, producing a solvent-free powder with the **1**β phase.

Preparation of a 1β-rich mixture of 1α and 1β

As-prepared **1** (80 mg) was placed in a glass vial (capacity of 5 mL), which was heated at 60 °C for 3 h in vacuo, resulting in a pre-mixed **1**β-rich solvent-free powder with the **1**α and **1**β phases.

Experimental procedure for selective encapsulation in the single-crystalline phase

As-prepared **1** (3 mg) and 2 mL of commercial grade *cis*- and *trans*-decalin mixture was mixed in a glass vial (capacity of 5 mL) at room temperature. The specimens were heated at 140 °C for 5 min by heating in an oil bath with stirring under an open-air atmosphere. Then, the heater was turned off to reach room temperature. The diffraction grade of the single crystals increased as the temperature gradually decreased.

Experimental procedure for selective encapsulation in the powder phase

As-prepared **1** (80 mg) was placed in a glass vial (capacity of 5 mL), which was placed in a larger glass vial (capacity of 50 mL) with 8 mL of a

cis- and *trans*-decalin mixture, *cis*-decalin, or *trans*-decalin. The larger glass vial was sealed tightly, and the specimens were left standing for 6 days. The resulting powders were subjected to PXRD analysis.

Experimental procedure for time-dependent PXRD measurements

The pre-mixed solvent-free powder with the **1**α and **1**β phases was placed on a glass plate. The specimen was placed on a glass stand in a desiccator (capacity of 500 mL). C*is*-decalin (300 mL) was poured into the desiccator. The desiccator containing the specimen was covered with a lid. The specimen was left standing at ambient temperature, and the aged specimen was subjected to PXRD measurements.

Experimental procedure for the gas sorption experiment

The N_2 gas sorption experiment was performed on a BELSORP-maxII034VP-MZ (MicrotracBEL). As-prepared **1** (30 mg) was heated at 60 °C for 3 h in vacuo to form the solvent-free powder with the **1**α and **1**β phases prior to the measurement. The N_2 isotherms were measured using a liquid nitrogen bath (77 K).

Data availability

All the data supporting the findings of this study are available within this article and in the Supplementary Information files. Additional data are available from the corresponding author upon request. The X-ray crystallographic coordinates for the structures reported in this study have been deposited at the Cambridge Crystallographic Data Centre (CCDC) under deposition numbers 2289472–2298477. These data can be obtained free of charge from the CCDC via www.ccdc.cam.ac.uk/data_request/cif.

References

1. Krause, S., Hosono, N. & Kitagawa, S. Chemistry of Soft Porous Crystals: Structural Dynamics and Gas Adsorption Properties. *Angew. Chem. Int. Ed.* **59**, 15325–15341 (2020).
2. Horike, S., Nagarkar, S. S., Ogawa, T. & Kitagawa, S. A New Dimension for Coordination Polymers and Metal–Organic Frameworks: Towards Functional Glasses and Liquids. *Angew. Chem. Int. Ed.* **59**, 6652–6664 (2020).
3. Kitagawa, S., Kitaura, R. & Noro, S.-i Functional Porous Coordination Polymers. *Angew. Chem. Int. Ed.* **43**, 2334–2375 (2004).
4. Yaghi, O. M. et al. Reticular synthesis and the design of new materials. *Nature* **423**, 705–714 (2003).
5. Côté, A. P. et al. Porous, Crystalline, Covalent Organic Frameworks. *Science* **310**, 1166–1170 (2005).
6. Wang, Z., Zhang, S., Chen, Y., Zhang, Z. & Ma, S. Covalent organic frameworks for separation applications. *Chem. Soc. Rev.* **49**, 708–735 (2020).
7. Freund, R. et al. The Current Status of MOF and COF Applications. *Angew. Chem. Int. Ed.* **60**, 23975–24001 (2021).
8. Cooper, A. I. Molecular Organic Crystals: From Barely Porous to Really Porous. *Angew. Chem. Int. Ed.* **51**, 7892–7894 (2012).
9. Lin, R.-B. et al. Multifunctional porous hydrogen-bonded organic framework materials. *Chem. Soc. Rev.* **48**, 1362–1389 (2019).
10. Li, P., Ryder, M. R. & Stoddart, J. F. Hydrogen-Bonded Organic Frameworks: A Rising Class of Porous Molecular Materials. *Acc. Mater. Res.* **1**, 77–87 (2020).
11. Martínez, C. & Corma, A. Inorganic molecular sieves: Preparation, modification and industrial application in catalytic processes. *Coord. Chem. Rev.* **255**, 1558–1580 (2011).
12. Dusselier, M. & Davis, M. E. Small-Pore Zeolites: Synthesis and Catalysis. *Chem. Rev.* **118**, 5265–5329 (2018).
13. Pérez-Botella, E., Valencia, S. & Rey, F. Zeolites in Adsorption Processes: State of the Art and Future Prospects. *Chem. Rev.* **122**, 17647–17695 (2022).
14. Yang, Y., Bai, P. & Guo, X. Separation of Xylene Isomers: A Review of Recent Advances in Materials. *Ind. Eng. Chem. Res.* **56**, 14725–14753 (2017).
15. O'Reilly, N., Giri, N. & James, S. L. Porous Liquids. *Chem. Eur. J.* **13**, 3020–3025 (2007).
16. Zhang, G. & Mastalerz, M. Organic cage compounds – from shape-persistency to function. *Chem. Soc. Rev.* **43**, 1934–1947 (2014).
17. Jie, K., Zhou, Y., Li, E. & Huang, F. Nonporous Adaptive Crystals of Pillararenes. *Acc. Chem. Res.* **51**, 2064–2072 (2018).
18. Little, M. A. & Cooper, A. I. The Chemistry of Porous Organic Molecular Materials. *Adv. Funct. Mater.* **30**, 1909842 (2020).
19. Wu, J.-R. & Yang, Y.-W. Synthetic Macrocycle-Based Nonporous Adaptive Crystals for Molecular Separation. *Angew. Chem. Int. Ed.* **60**, 1690–1701 (2021).
20. Zhang, G. et al. Intrinsically Porous Molecular Materials (IPMs) for Natural Gas and Benzene Derivatives Separations. *Acc. Chem. Res.* **54**, 155–168 (2021).
21. Zhang, G., Lin, W., Huang, F., Sessler, J. & Khashab, N. M. Industrial Separation Challenges: How Does Supramolecular Chemistry Help? *J. Am. Chem. Soc.* **145**, 19143–19163 (2023).
22. Barbour, L. J. Crystal porosity and the burden of proof. *Chem. Commun.* **21**, 1163–1168 (2006).
23. Atwood, J. L., Barbour, L. J., Jerga, A. & Schottel, B. L. Guest Transport in a Nonporous Organic Solid via Dynamic van der Waals Cooperativity. *Science* **298**, 1000–1002 (2002).
24. Steed, J. W. Molecular "Ghosts". *Science* **298**, 976–977 (2002).
25. Atwood, J. L., Barbour, L. J. & Jerga, A. Storage of Methane and Freon by Interstitial van der Waals Confinement. *Science* **296**, 2367–2369 (2002).
26. Enright, G. D., Udachin, K. A., Moudrakovski, I. L. & Ripmeester, J. A. Thermally Programmable Gas Storage and Release in Single Crystals of an Organic van der Waals Host. *J. Am. Chem. Soc.* **125**, 9896–9897 (2003).
27. Atwood, J. L., Barbour, L. J. & Jerga, A. A New Type of Material for the Recovery of Hydrogen from Gas Mixtures. *Angew. Chem. Int. Ed.* **43**, 2948–2950 (2004).
28. Atwood, J. L., Barbour, L. J., Thallapally, P. K. & Wirsig, T. B. A crystalline organic substrate absorbs methane under STP conditions. *Chem. Commun.* **7**, 51–53 (2005).
29. Thallapally, P. K. et al. Acetylene Absorption and Binding in a Nonporous Crystal Lattice. *Angew. Chem. Int. Ed.* **45**, 6506–6509 (2006).
30. Dalgarno, S. J., Thallapally, P. K., Barbour, L. J. & Atwood, J. L. Engineering void space in organic van der Waals crystals: calixarenes lead the way. *Chem. Soc. Rev.* **36**, 236–245 (2007).
31. Brouwer, D. H., Moudrakovski, I. L., Udachin, K. A., Enright, G. D. & Ripmeester, J. A. Guest Loading and Multiple Phases in Single Crystals of the van der Waals Host p- tert-Butylcalix[4]arene. *Cryst. Growth Des.* **8**, 1878–1885 (2008).
32. Udachin, K. A., Moudrakovski, I. L., Enright, G. D., Ratcliffe, C. I. & Ripmeester, J. A. Loading-dependent structures of CO2 in the flexible molecular van der Waals host p-tert-butylcalix[4]arene with 1:1 and 2:1 guest–host stoichiometries. *Phys. Chem. Chem. Phys.* **10**, 4636–4643 (2008).
33. Morohashi, N. et al. Inclusion of Alkanes with a Crystal Consisting of Exocavity Complexes of p-tert-Butylthiacalix[4]arene with Diethylamine: Extension of Guest Scope by Changing the Structure of Inclusion Crystals. *Cryst. Growth Des.* **19**, 7022–7029 (2019).
34. Kitaigorodskii, A. The principle of close packing and the condition of thermodynamic stability of organic crystals. *Acta Crystallogr.* **18**, 585–590 (1965).
35. Hasell, T. & Cooper, A. I. Porous organic cages: soluble, modular and molecular pores. *Nat. Rev. Mater.* **1**, 16053 (2016).

36. Kato, K., Hiroi, T., Seto, N., Ohtani, S. & Ogoshi, T. Selective Gas Adsorption on Molecular Solids of a Hydrogen-bonding [3.3.3] Propellane. *Chem. Lett.* **51**, 975–977 (2022).
37. Kato, K. et al. Synthesis of Hexa-Aminated Trinaphtho[3.3.3]propellane and Its Porous Polymer Solids with Alkane Adsorption Properties. *Bull. Chem. Soc. Jpn.* **95**, 1296–1302 (2022).
38. Rahmani, M. et al. Highly Selective p-Xylene Separation from Mixtures of C8 Aromatics by a Nonporous Molecular Apohost. *J. Am. Chem. Soc.* **145**, 27316–27324 (2023).
39. Haino, T. & Hirao, T. Supramolecular Polymerization and Functions of Isoxazole Ring Monomers. *Chem. Lett.* **49**, 574–584 (2020).
40. Ikeda, T. & Haino, T. Supramolecular polymeric assemblies of π-conjugated molecules possessing phenylisoxazoles. *Polymer* **128**, 243–256 (2017).
41. Huber, R. G. et al. Heteroaromatic π-Stacking Energy Landscapes. *J. Chem. Inf. Modeling* **54**, 1371–1379 (2014).
42. Ragini, Ranjan, R., Mishra, S. K. & Pandey, D. Room temperature structure of Pb(ZrxTi1−xO3) around the morphotropic phase boundary region: A Rietveld study. *J. Appl. Phys.* **92**, 3266–3274 (2002).
43. Inokuma, Y. et al. X-ray analysis on the nanogram to microgram scale using porous complexes. *Nature* **495**, 461–466 (2013).
44. Jie, K. et al. Styrene Purification by Guest-Induced Restructuring of Pillar[6]arene. *J. Am. Chem. Soc.* **139**, 2908–2911 (2017).
45. Jie, K. et al. Near-Ideal Xylene Selectivity in Adaptive Molecular Pillar[n]arene Crystals. *J. Am. Chem. Soc.* **140**, 6921–6930 (2018).
46. Matsumoto, T. et al. What is This?" A Structure Analysis Tool for Rapid and Automated Solution of Small Molecule Structures. *J. Chem. Crystallogr.* **51**, 438–450 (2021).
47. Seyer, W. F. & Mann, C. W. The Vapor Pressures of cis- and trans-Decahydronaphthalene. *J. Am. Chem. Soc.* **67**, 328–329 (1945).
48. Bayón, C. et al. Direct Enzymatic Branch-End Extension of Glycocluster-Presented Glycans: An Effective Strategy for Programming Glycan Bioactivity. *Chem. Eur. J.* **23**, 1623–1633 (2017).
49. Jiang, K.-M., Zhang, J.-Q., Jin, Y. & Lin, J. 1,3-Dipolar Cycloaddition of Imidazole Derivatives with Nitrile Oxide: Synthesis of Imidazo[1,2,4]oxadiazole Derivatives. *Asian J. Org. Chem.* **6**, 1620–1627 (2017).
50. Dolomanov, O. V., Bourhis, L. J., Gildea, R. J., Howard, J. A. K. & Puschmann, H. J. OLEX2: a compete structure solution, refinement and analysis program. *Appl. Cryst.* **42**, 339–341 (2009).
51. Sheldrick, G. M. A short histry of SHELX. *Acta Cryst.* **A64**, 112–122 (2008).
52. Sheldrick, G. M. SHELXT – Integrated space-group and crystal-structure determination. *Acta Cryst.* **A71**, 3–8 (2015).
53. Sheldrick, G. M. Crystal structure refinement with SHELXL. *Acta Cryst.* **C71**, 3–8 (2015).
54. Spackman, P. R. et al. CrystalExplorer: a program for Hirshfeld surface analysis, visualization and quantitative analysis of molecular crystals. *J. Appl. Cryst.* **54**, 1006–1011 (2021).

Acknowledgements

The authors are grateful to Ms. Tomoko Amimoto and Mr. Hitoshi Fujitaka, the Natural Science Center for Basic Research Development (N-BARD), Hiroshima University, for the NMR and HRMS measurements, respectively. The authors thank Dr. Toshimi Nakaya, Mr. Ohashi Toshihiko, and Ms. Michiko Ujihara, Division of Materials Model-Based Research Digital Monodzukuri (Manufacturing) Education and Research Center, Hiroshima University, for the gas sorption experiments. This work was supported by JSPS KAKENHI, Grants-in-Aid for Transformative Research Areas, "Condensed Conjugation" Grant Number JP21H05491 and "Materials Science of Meso-Hierarchy" Grant Number JP23H04873 to T. Haino, Grant-in-Aid for Scientific Research (A) Grant Number JP21H04685 to T. Haino, and Grant-in-Aid for Young Scientists Grant Number JP22K14727 to T. Hirao. We also acknowledge support from the KEIRIN JKA, Grant Number 2023 M-419 to T. Haino, and JST for the establishment of university fellowships toward the creation of science technology innovation (JPMJFS2129 to Y.O.). Funding from the Toshiaki Ogasawara Memorial Foundation, Tobe Maki Scholarship Foundation, Urakami Scholarship Foundation, Proterial Materials Science Foundation, ENEOS Tonengeneral Research/Development Encouragement & Scholarship Foundation, Takahashi Industrial and Economic Research Foundation, and Furukawa Foundation for Promotion of Technical Science is gratefully acknowledged.

Author contributions

T. Haino conceived the project. Y. Ono and T. Hirao designed the experiments. Y. Ono, T. Hirao, and T. Haino wrote the manuscript. Y. Ono synthesized the molecule studied in this project. Y. Ono and N. Kawata performed the crystallographic study. Y. Ono and T. Hirao contributed equally. All authors discussed the results and commented on the manuscript.

Competing interests

The authors declare no competing interests.

Additional information

Supplementary information The online version contains supplementary material available at https://doi.org/10.1038/s41467-024-52526-9.

Correspondence and requests for materials should be addressed to Takeharu Haino.

Peer review information *Nature Communications* thanks Vincent J. Smith, Ruqiang Zou and the other, anonymous, reviewer(s) for their contribution to the peer review of this work. A peer review file is available.

Reprints and permissions information is available at http://www.nature.com/reprints

Publisher's note Springer Nature remains neutral with regard to jurisdictional claims in published maps and institutional affiliations.

Open Access This article is licensed under a Creative Commons Attribution-NonCommercial-NoDerivatives 4.0 International License, which permits any non-commercial use, sharing, distribution and reproduction in any medium or format, as long as you give appropriate credit to the original author(s) and the source, provide a link to the Creative Commons licence, and indicate if you modified the licensed material. You do not have permission under this licence to share adapted material derived from this article or parts of it. The images or other third party material in this article are included in the article's Creative Commons licence, unless indicated otherwise in a credit line to the material. If material is not included in the article's Creative Commons licence and your intended use is not permitted by statutory regulation or exceeds the permitted use, you will need to obtain permission directly from the copyright holder. To view a copy of this licence, visit http://creativecommons.org/licenses/by-nc-nd/4.0/.

© The Author(s) 2024